文章编号：1001-9014(XXXX)XX-0001-08

DOI:10.11972/j.issn.1001-9014.XXXX.XX.001

High-Performance Terahertz Detectors Based on Large-Area Semimetallic Platinum Telluride ($PtTe_2$)

HUANG De-Bao[1,2], ZHOU Wei[2], HUANG Jing-Guo[2], QIU Qin-Xi[2], JIANG Lin[2], YAO Niang-Juan[2], GAO Yan-Qing[2], HUANG Zhi-Ming[1,2*]

(1. Shanghai University, School of Microelectronics, 20 Cheng Zhong Road, Shanghai 200444, People's Republic of China.;
2. State Key Laboratory of Infrared Physics, Shanghai Institute of Technical Physics, Chinese Academy of Sciences, 500 Yu Tian Road, Shanghai 200083, People's Republic of China.)

Abstract: Terahertz (THz) detectors, serving as the pivotal components for photoelectric conversion, constitute one of the fundamental building blocks in modern information society. Large-area $PtTe_2$ thin films were synthesized via chemical vapor deposition (CVD), enabling the fabrication of THz detectors with varied channel lengths. Characterization results demonstrate that the device response exhibits linear dependence on both bias voltage and incident power, while the responsivity shows an inverse proportionality to channel length and operational frequency. The observed device characteristics align well with theoretical calculations based on the electromagnetic induced well (EIW) mechanism. Notably, EIW-based devices achieve a rapid response time of ~7.6 μs, with noise equivalent power (NEP) below 7.9×10^{-15} W/Hz$^{0.5}$ and specific detectivity (D*) exceeding 9×10^{10} cm·Hz$^{0.5}$/W under limited bias conditions. These performance metrics surpass those of previously reported semimetallic $PtTe_2$-based detectors.

Key words: terahertz, detectors, platinum telluride, electromagnetic induced well
PACS:

基于大面积半金属碲化铂的高性能太赫兹探测器

黄德宝[1,2], 周 炜[2], 黄敬国[2], 邱琴茜[2], 江 林[2], 姚娘娟[2], 高艳卿[2], 黄志明[1,2*]

(1. 上海大学 微电子学院,上海 200444;
2. 中国科学院上海技术物理研究所 红外科学与技术全国重点实验室,上海 200083)

摘要:太赫兹(THz)探测器是实现光电转换的核心,是现代信息社会的基础之一。基于CVD法生长了大面积$PtTe_2$薄膜,制备了不同沟道长度的太赫兹探测器。对器件的测试结果表明,器件响应与偏置电压和功率呈线性相关,响应率与沟道长度和频率呈负相关。器件出现的特征与基于电磁诱导势阱(EIW)效应的计算结果一致。基于EIW效应的器件具有~7.6微秒的快速响应时间,在有限偏置下的噪声等效功率(NEP)优于7.9×10^{-15} W/Hz$^{0.5}$,比探测率D*优于9×10^{10} cm·Hz$^{0.5}$/W,优于目前已报道的基于半金属$PtTe_2$的探测器。

关 键 词:太赫兹;探测器;碲化铂;电磁诱导势阱

中图分类号:O43　　**文献标识码**:A

Received date: 2025-04-09, **revised date**: 2025-04-23　　**收稿日期**:2025-04-09,**修回日期**:2025-04-23

Foundation items: Supported by the National Natural Science Foundation of China (Grant Nos. 52071329, 12134016); Youth Innovation Promotion Association, CAS (Grant No. 2022240) Strategic Priority Research Program of the Chinese Academy of Sciences (Grant No. XDB0580000); Open Fund of State Key Laboratory of Infrared Physics (Grant No. SITP-NLIST-YB-2023-08); Shanghai Municipal Science and Technology Yangfan Special Project (Grant No. 23YF1455300)

Biography: HUANG De-Bao (1999-), male, Bazhong, Sichuan Province, master. Research area involves Terahertz detection materials and devices. E-mail:413731663@qq.com.

* **Corresponding author**: E-mail: zmhuang@mail.sitp.ac.cn

Introduction

The investigation of terahertz (THz) radiation applications has emerged as a highly active and interdisciplinary frontier of rapid development, with numerous fundamental discoveries and practical implementations continuously emerging. THz radiation enables the detection and manipulation of quasiparticles and collective excitations in solids, facilitates the driving of phase transitions and associated material property modifications, and provides insights into rotational and vibrational dynamics in molecular systems[1]. Owing to its abundant bandwidth, reduced latency, and enhanced data transmission rates spanning from Gbps to Tbps, the THz band is regarded as an ideal candidate for next-generation 6G communications[2]. Furthermore, the non-ionizing nature of THz waves coupled with their superior penetration capability through non-conductive materials (e. g. , ceramics and plastics) enables wide-ranging applications in non-destructive testing[3], biomedical diagnostics[4, 5], and food quality control industries[6]. High-performance photodetectors[7], serving as critical transducers converting optical signals into electrical responses, constitute the essential foundation for realizing these practical applications. In the exploration of photoelectric materials, two-dimensional (2D) materials have garnered significant research interest due to their tunable bandgaps[8, 9], ultrahigh carrier mobility[10, 11] with rapid response characteristics, atomic-scale thickness enabling strong light-matter interactions, and exceptional integration flexibility through van der Waals (vdW) heterostructuring[12].

Among these, transition metal dichalcogenides (TMDs) have attracted particular attention owing to their adjustable conductivity and spin-orbit coupling[13]. As a representative transition metal dichalcogenide, $PtTe_2$ exhibits unique topological characteristics revealed by angle-resolved photoemission spectroscopy (ARPES) and first-principles calculations[14]. These studies identify a pair of strongly tilted Dirac cones along the Γ-A direction, confirming $PtTe_2$ as a type-II Dirac semimetal. The topologically non-trivial Z_2 invariant induces spin-momentum-locked topological surface states, analogous to those observed in topological insulators. Owing to its exceptional chemical stability[15-17], mechanical flexibility[18], thermal robustness[19], and high electrical conductivity, $PtTe_2$ has attracted extensive research interest. Pioneering studies by J. B. McManus et al. demonstrated the synthesis of $PtTe_2$ thin films via solid-phase precursor reactions, which exhibited superior electrocatalytic performance in hydrogen evolution reaction and oxygen reduction reaction[20]. D. Kireev et al. developed ultrathin electronic tattoos using large-scale synthesized $PtTe_2$ layers for real-time monitoring of human physiological signals, including cardiac/brain electrical activities, muscular contractions, ocular movements, and body temperature, highlighting its potential in wearable healthcare and flexible electronics[21]. E. Okogbue et al. achieved centimeter-scale growth of 2D $PtTe_2$ on glass substrates, demonstrating its applications in thermochromic displays and electrically activated defogging windows through efficient electrothermal conversion[22]. Layer-dependent electronic transitions were revealed by M. -K. Lin et al. via reflection high-energy electron diffraction (RHEED) and ARPES analyses, showing a thickness-driven semimetal-to-semiconductor transition with a 0. 79 eV indirect bandgap in monolayer $PtTe_2$[23]. Notably, H. Xu et al. reported giant spin Hall conductivity in semimetallic $PtTe_2$ films originating from the synergistic effects of large spin-orbit torque (SOT) efficiency and high electrical conductivity, positioning it as an ideal candidate for low-power spintronic devices[24].

As a photosensitive material, $PtTe_2$-based photodetectors and heterostructures have achieved broadband detection spanning visible to THz regimes[25-27]. However, the underlying THz response mechanisms remain controversial. K. Zhang et al. attributed the THz photoresponse to the photothermoelectric (PTE) effect in interdigital antenna-integrated devices[28], while A. Jakhar et al. proposed dual contributions from photo-galvanic and photon-drag effects[29]. Z. Dong et al. emphasized strong THz-carrier coupling enabled by tilted Dirac cones near the Fermi surface[30], whereas L. Zhang et al. correlated the photocurrent with topological surface states and surface plasmon polariton (SPP)-induced non-equilibrium carriers in log-periodic antenna architectures[31].

This study demonstrates THz detectors fabricated from large-area $PtTe_2$ thin films grown via chemical vapor deposition (CVD), with systematically varied channel lengths. The observed responsivity dependencies on both channel length (5-10 μm) and operational frequency (0. 02-0. 173 THz) align with theoretical predictions of the electromagnetic induced well (EIW) mechanism. The linear photocurrent-voltage and photocurrent-power relationships further validate EIW-dominated response characteristics. Remarkably, EIW-activated devices achieve ultrafast response times (~7 μs), with noise equivalent power (NEP) $<10^{-14}$ $W \cdot Hz^{-0.5}$ and specific detectivity (D*) $>10^{10}$ $cm \cdot Hz^{0.5} \cdot W^{-1}$ under moderate bias conditions, representing a new benchmark for semimetallic THz detectors.

1 Experiments

The fabrication process of high-quality $PtTe_2$ thin films is illustrated in Figure 1a. Chemically vapor-transported (CVT) $PtTe_2$ crystals were employed as the evaporation source, supplemented with elemental tellurium (Te) as an auxiliary chalcogen precursor. The growth was conducted in a three-zone chemical vapor deposition (CVD) furnace under precisely controlled thermal gradients. Ultra-high purity argon (100 sccm) and hydrogen (20 sccm) served as carrier gases. Precursor materials were strategically positioned: 0. 5 g Te powder in the upstream zone (550 °C), 0. 1 g $PtTe_2$ powder in the central high-temperature zone (750 °C), and sapphire substrates in the downstream zone (600 °C). After 15-minute growth, uniform $PtTe_2$ films were obtained on sapphire substrates, which were subsequently transferred onto SiO_2/Si substrates via a polymethyl methacrylate (PMMA)-assisted stamping method.

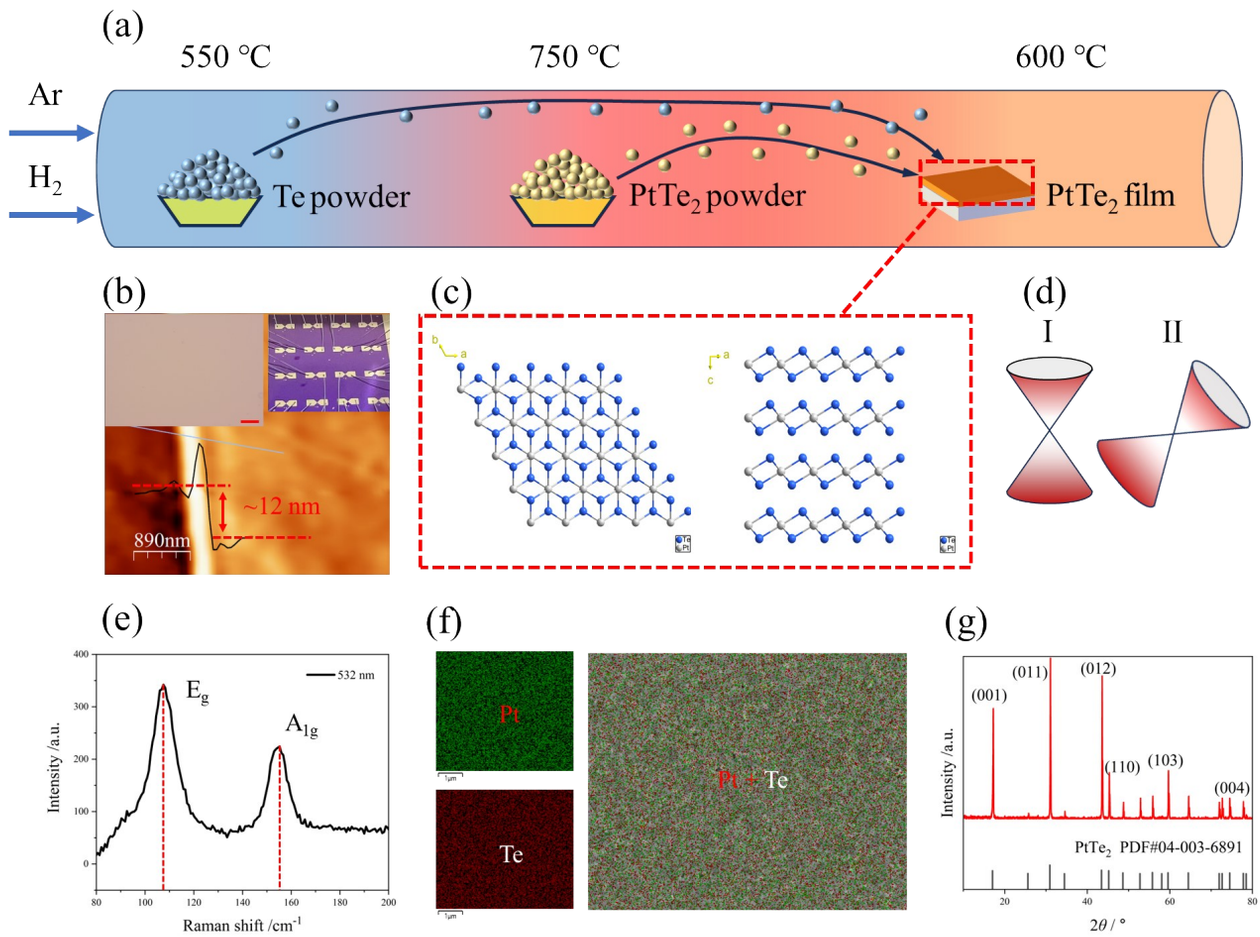

图 1　材料生长及表征结果：(a)碲化铂薄膜材料生长示意图；(b)薄膜的 AFM 测试结果，左上角插图为光学显微镜下的薄膜，标尺为 100 微米，右上角所示为使用生长材料制备的 4×4 器件阵列；(c)碲化铂的晶体结构；(d)I型狄拉克锥与碲化铂的II型狄拉克锥能带结构；(e)薄膜的拉曼测试结果；(f)对薄膜表面的 EDS 测试结果；(g)对材料的 x 射线衍射图谱

Fig. 1　Material growth and characterization results: (a) Schematic of $PtTe_2$ thin-film growth process; (b) Atomic force microscopy (AFM) characterization of the thin film. Top-left inset: Optical microscopy image (scale bar: 100 μm). Top-right inset: 4×4 device array fabricated from the as-grown material. ; (c) Crystal structure of $PtTe_2$; (d) Type-I Dirac cone versus type-II Dirac cone band structures in platinum telluride ($PtTe_2$); (e) Raman spectroscopy analysis; (f) EDS elemental mapping of the film surface; (g) X-ray diffraction (XRD) pattern of the material

Device fabrication involved ultraviolet (UV) photolithography to define the active sensing area, followed by selective etching using aqua regia (HCl: HNO_3 = 3: 1 vol%) to remove excess material. A secondary lithography step patterned the electrode regions, where Cr/Au (15 nm/70 nm) were deposited via dual-ion beam sputtering. The final architecture was achieved through standard lift-off processing in acetone, completing the metal-semimetal contact formation.

1 Results and discussions

Atomic force microscopy (AFM) measurements of the as-grown $PtTe_2$ film reveal a thickness of approximately 12 nm (Figure 1b). The corresponding optical microscopy image shown in the inset demonstrates excellent thickness homogeneity through uniform optical contrast. The crystal structure of $PtTe_2$, illustrated in Figure 1c, adopts a CdI_2-type trigonal (1T) configuration with P3m1 space group (No. 164), comprising edge-sharing $PtTe_6$ octahedra forming stacked $PtTe_2$ layers along the ab-plane. The lattice parameters were determined as a = b = 4. 03 Å and c = 5. 22 Å. Distinct from the Lorentz-invariant type-I Dirac cones in graphene, $PtTe_2$ exhibits Lorentz-violating type-II Dirac fermions with tilted Dirac cones[14] (Figure 1d).

Raman spectroscopy characterization (Figure 1e) reveals two prominent phonon modes within 80-200 cm^{-1}: The peak at ~111 cm^{-1} corresponds to the E_g mode arising from in-plane Te - Pt - Te vibrations, while the ~158 cm^{-1} feature originates from out-of-plane A_{1g} vibrations of Te atoms, attributed to displacive excitation of coherent phonons (DECP)[32]. Figure 1f displays the energy-dispersive X-ray spectroscopy (EDS) elemental mapping, demonstrating homogeneous spatial distributions of plati-

num (Pt) and tellurium (Te). Furthermore, the X-ray diffraction (XRD) pattern in Figure 1g exhibits sharp diffraction peaks, confirming the well-crystallized nature of the CVD-grown $PtTe_2$ thin film.

The EIW effect represents a novel photoconductive mechanism[33], enabling high-sensitivity room-temperature THz detection with incident photon energies far below the material bandgap through subwavelength-channel-length metal-semiconductor-metal (MSM) structures[34, 35]. Figure 2a schematically illustrates the EIW operational principle.

When THz waves illuminate the MSM structure with subwavelength channel length, the Lorentz force drives electron injection from metallic electrodes into the $PtTe_2$ channel, forming carrier accumulation regions through potential well modulation. This carrier density redistribution alters the material conductivity, generating detectable photocurrent under external bias (V_b). The theoretical model predicts the EIW-induced carrier concentration as:

$$\Delta n = \frac{4\varepsilon_0 \eta P \tau_e \mu}{\pi^3 e^2 d c_0 \sqrt{\varepsilon_r}} \sqrt{\left(\frac{\pi}{a}\right)^2 - k_0^2} \times \left[1 - \exp\left(-d\sqrt{\varepsilon_r}\sqrt{\left(\frac{\pi}{a}\right)^2 - k_0^2}\right)\right] \tag{1}$$

Where ε_0=8.854×10^{-12} F/m (vacuum permittivity), P denotes incident power, τ_e represents carrier lifetime, e = 1.602×10^{-19} C (elementary charge), d is $PtTe_2$ thickness, c_0= 3×10^8 m/s (light speed), ε_r represents the relative permittivity, and $k_0 = \frac{2\pi f}{c_0}$ (free-space wavevector). The field enhancement factor $\eta = \left|\frac{\varepsilon(\omega)\sqrt{k_0^2 - \left(\frac{\pi}{a}\right)^2}}{\sqrt{\varepsilon(\omega)k_0^2 - \left(\frac{\pi}{a}\right)^2}}\right|$ incorporates Au electrode permittivity $\varepsilon(\omega)$= 1.13×10^5.

Under constant bias V_b, the photocurrent relates to Δn through:

$$I_{ph} = \frac{\Delta n}{n} \cdot \frac{V_b}{R} \tag{2}$$

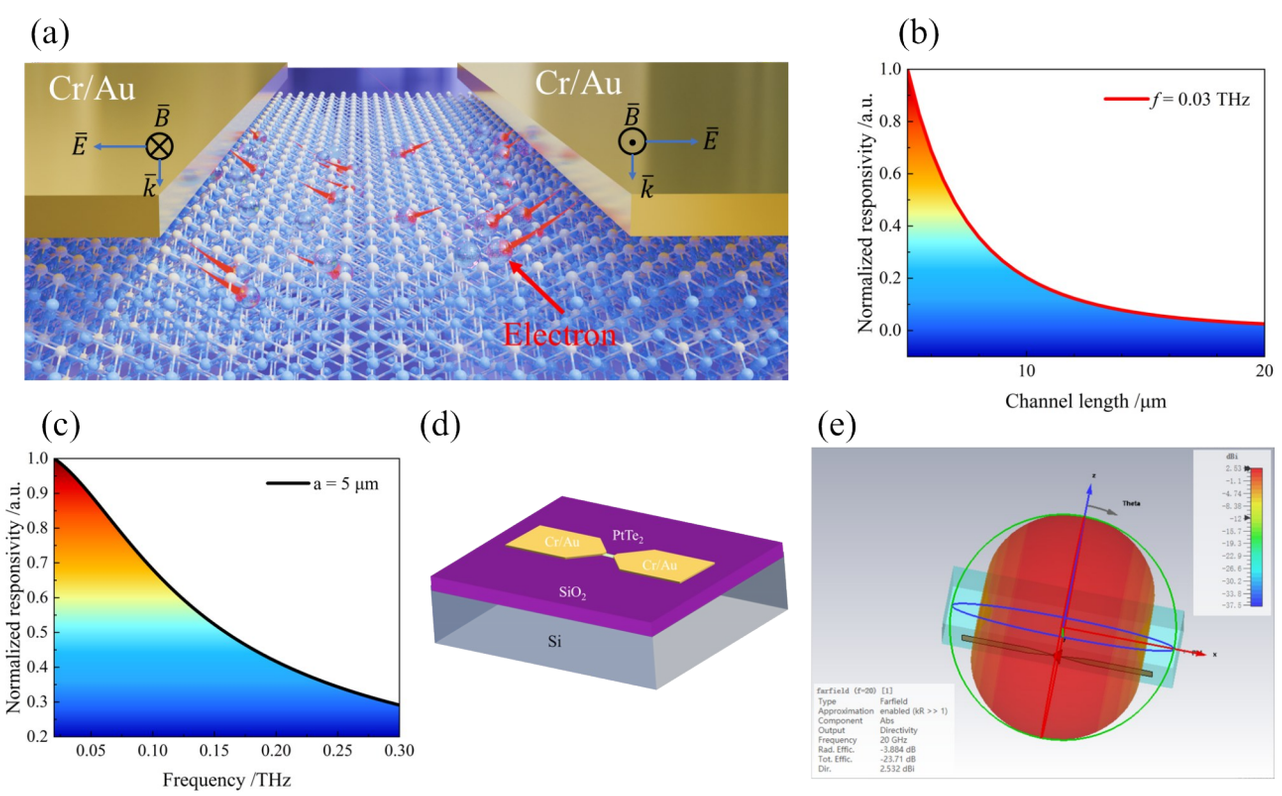

图2 太赫兹探测机制及相应计算和仿真结果:(a)电磁诱导势阱效应原理示意图;(b)EIW效应响应率与沟道长度的依赖关系;(c)EIW效应响应率与频率的依赖关系;(d)所采用的器件结构示意图;(e)对天线的电磁仿真结果

Fig. 2 THz detection mechanism and corresponding calculation and simulation results: (a) Operational principle of the electromagnetic induced well (EIW) effect; (b) Responsivity dependence on channel length under EIW mechanism; (c) Frequency-dependent responsivity characteristics; (d) Schematic of device architecture; (e) Electromagnetic simulation results of antenna performance

Combining Equations (1) and (2) yields the theoretical current responsivity:

$$R_i = \frac{I_{ph}}{P} = \frac{4\varepsilon_0 E_0 \eta V_b \tau_e \mu}{\pi^3 e^2 dnc_0 R\sqrt{\varepsilon_r}} \sqrt{\left(\frac{\pi}{a}\right)^2 - k_0^2} \times \left[1 - \exp\left(-d\sqrt{\varepsilon_r}\sqrt{\left(\frac{\pi}{a}\right)^2 - k_0^2}\right)\right] \quad (3)$$

where E_0 denotes free-space electric field. As theoretically predicted by Equation (3), the responsivity exhibits distinct dependencies on both channel length and operational frequency, as systematically demonstrated in Figures 2b and 2c, respectively. Quantitative analysis reveals an approximately 80% degradation in responsivity when scaling the channel length from 5 μm to 10 μm under a 0.1 V bias. Concurrently, an approximately 60% reduction occurs as the frequency increases from 0.02 THz to 0.165 THz.

The metallic electrodes in practical devices serve dual functionalities: (i) as electrical contact pads for external circuitry interconnection, and (ii) as bow-tie antennas for THz wave coupling enhancement. To decouple the antenna contribution, electromagnetic simulations were performed on the structure depicted in Figure 2d. The simulation results in Figure 2e quantify a 2.5 dBi gain (G = 1.5) at 0.02 THz, confirming effective electromagnetic field confinement through electrode engineering.

DC current-voltage (I-V) characteristics of devices with 5 μm and 10 μm channel lengths are presented in Figure 3a. The linear Ohmic behavior confirms superior metal-semimetal interfaces, essential for photoconductive detectors, while the low series resistance corroborates the inherent semimetallic nature of $PtTe_2$. The photoresponse characterization system (Figure 3b) employs a modulated THz source illuminating the device mounted on a PCB. Synchronized lock-in amplification with signal modulation frequency ensures precise detection, where the photoresponse is amplified by a preamplifier and recorded via computer-controlled data acquisition. Real-time waveform monitoring using an oscilloscope enables response speed evaluation. Incident power density calibration is achieved through a Golay detector or power meter positioned equivalently.

Responsivity (R_i), defined as photocurrent per unit incident power ($R_i = \frac{I_{ph}}{P \cdot G}$), was systematically quanti-

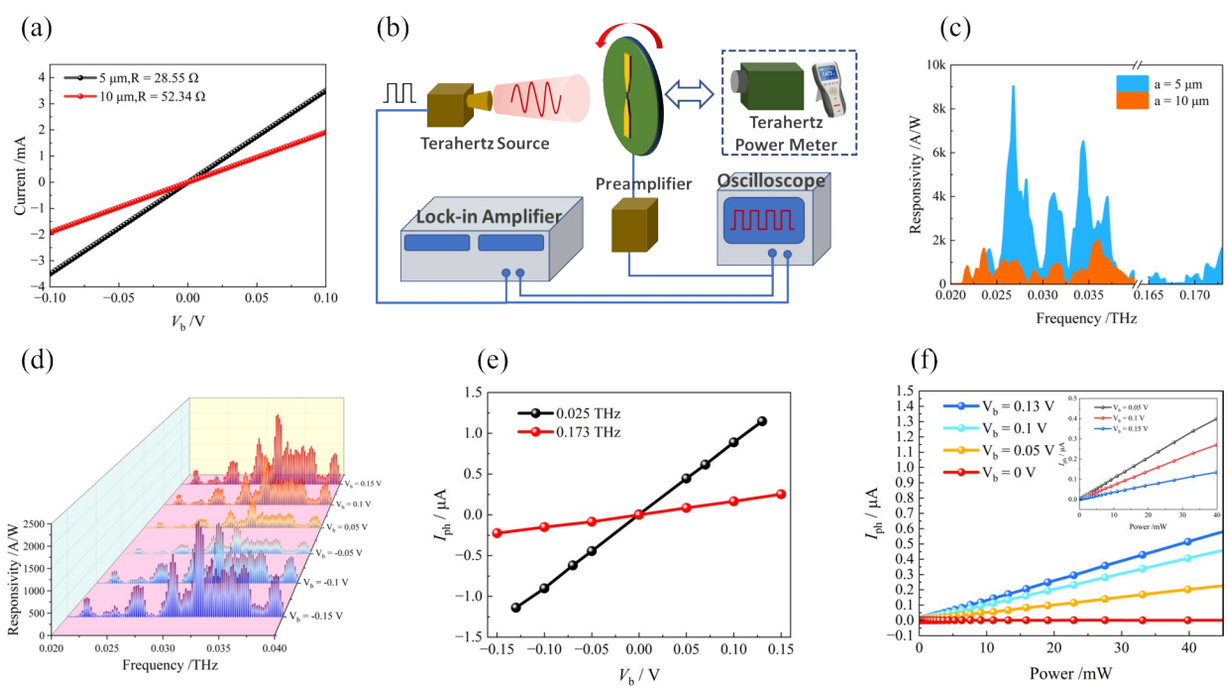

图3 测试系统及器件光电响应特性说明:(a)不同沟道长度器件的电流-电压特性曲线;(b)器件响应测试系统示意图;(c)在0.1 V偏置电压下不同沟道的器件对不同频段的太赫兹辐射的响应率测试结果;(d)沟道长度为10微米的器件在不同偏置电压下的响应图谱;(e)器件在不同频率下的线性光电流-偏置电压特性曲线;(f)器件在不同偏置电压下光电流与输出功率的线性依赖关系(插图为10微米沟道长度)

Fig. 3 Testing system and device photoelectric response characteristics description: (a) Current-voltage (I-V) characteristics of devices with different channel lengths; (b) Schematic of photoresponse measurement system; (c) Responsivity spectra across 0.02-0.04 THz and 0.165-0.173 THz bands at 0.1 V bias; (d) Bias-dependent responsivity of 10 μm-channel devices; (e) Linear photocurrent-bias voltage characteristics under 0.025/0.173 THz illumination; (f) Photocurrent-power linearity under varying biases (inset: 10 μm-channel data)

fied. Here, I_{ph} denotes photocurrent, $P = P_0 \cdot S_0$ (P_0: power density; S_0: active area ≈ channel area due to oversize illumination), and G represents antenna gain.

Figure 3c demonstrates frequency-dependent responsivity in 0.02-0.04 THz and 0.165-0.173 THz bands. The 5 μm-channel device achieves peak R_i ~ 9000 A/W at 0.02-0.04 THz, exhibiting ~77% and ~82% reductions with channel elongation to 10 μm and frequency up-conversion to 0.165-0.173 THz, respectively - in excellent agreement with EIW theoretical predictions.

Equation (2) explicitly establishes the linear I_{ph}-V_b relationship ($I_{ph} \propto V_b$), validated by the bias-dependent photocurrent enhancement with reproducible spectral features in Figure 3d. The preserved linearity under both 0.025 THz and 0.173 THz illumination across positive/negative biases (Figure 3e) further confirms this proportionality. Figure 3f illustrates strict linear I_{ph}-P dependence for 5 μm-channel devices (10 μm inset), where constant slopes align with EIW theory through $\Delta n \propto P$ (Equation 1) and $I_{ph} \propto \Delta n$ (Equation 2). This comprehensive consistency unequivocally attributes the photoresponse to the EIW mechanism.

The temporal response characteristics under 0.1 V DC bias were captured via oscilloscopic measurements (Figure 4a). The rise time (τ_r) and fall time (τ_f), defined as the durations required for the signal to transition between 10%-90% and 90%-10% of the maximum steady-state value respectively, were determined as $\tau_r \approx 7.56$ μs and $\tau_f \approx 7.74$ μs. The 3 dB bandwidth illustrated in Figure 4b further corroborates the rapid response, with microsecond-scale dynamics significantly outperforming commercial detectors including Golay cells, pyroelectric sensors, and uncooled bolometers. This ultrafast performance underscores the device's potential for real-time imaging applications in security screening, ther-

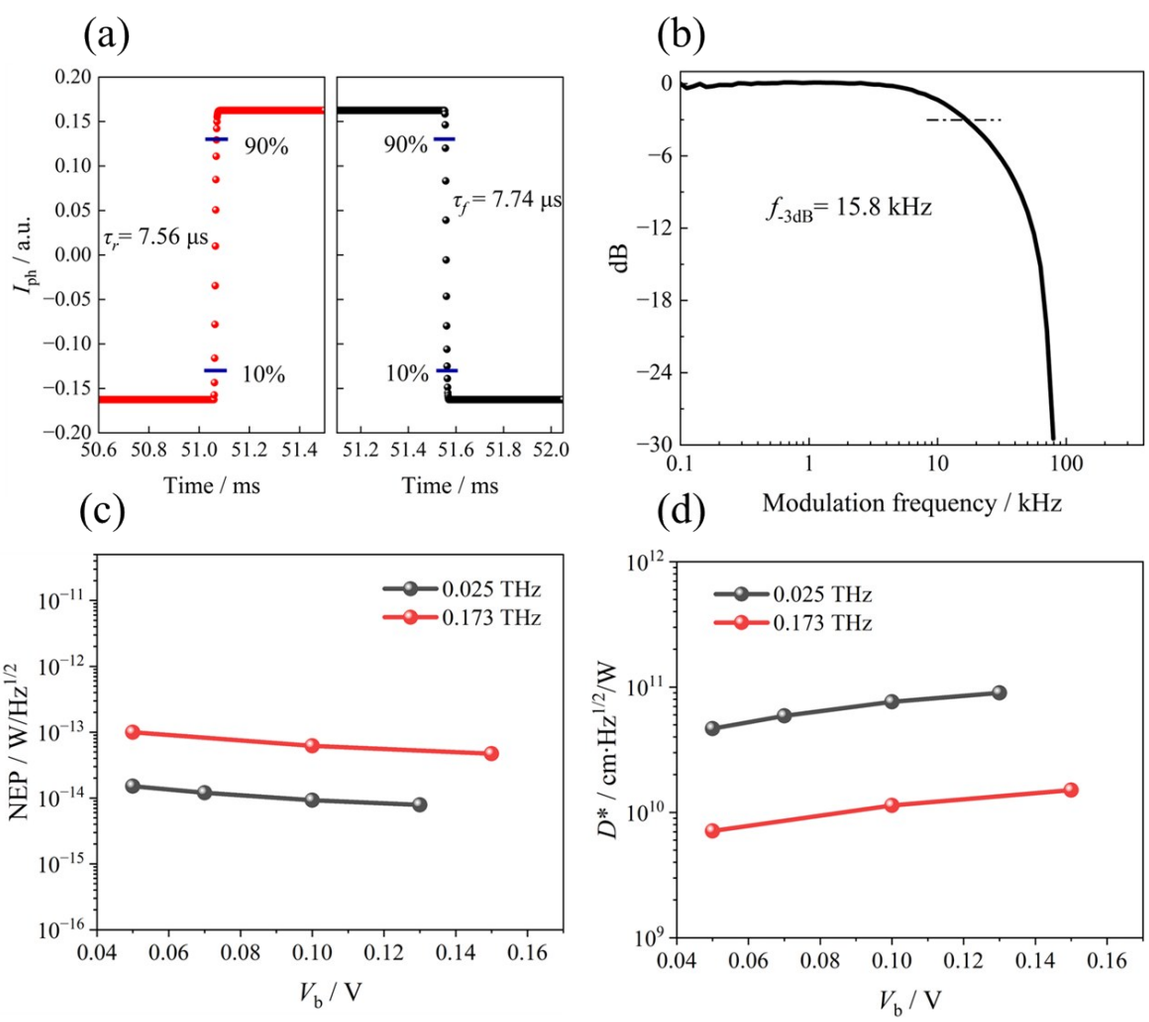

图4 室温下基于EIW效应的器件性能:(a)使用示波器测量的器件的响应特性;(b)器件光响应随调制频率的关系;(c)不同频率下器件噪声等效功率随偏置电压的关系;(d)不同频率下器件比探测率随偏置电压的关系

Fig. 4 Device performance based on EIW effect at room temperature: (a) Temporal response characteristics measured by oscilloscope; (b) Modulation frequency-dependent photoresponse roll-off; (c) Bias-voltage evolution of noise equivalent power (NEP) at different frequencies; (d) Specific detectivity (D*) versus bias voltage at different frequencies

mography, and non-destructive evaluation. Detector sensitivity is typically quantified by the noise equivalent power (NEP), defined as the input power required to achieve unity signal-to-noise ratio (SNR = 1) within 1 Hz bandwidth: $NEP = \frac{i_n}{R_i}$, where lower NEP values indicate superior sensitivity. The dominant noise components comprise: flicker (1/f) noise: negligible at modulation frequencies >1 kHz, Johnson-Nyquist noise: $i_{jn} = \sqrt{\frac{4K_BT}{R}}$, shot noise: $i_{sn} = \sqrt{2eI_d}$. The resultant noise current follows: $i_n = \sqrt{i_{jn}^2 + i_{sn}^2}$. As shown in Figure 4c, the device achieves NEP ~10^{-14} W·$Hz^{-0.5}$ at 0.1 V bias, with slight improvement at higher biases. More comprehensively, the specific detectivity: $D^* = \frac{\sqrt{S_0}}{NEP}$ normalizes performance across active areas. The bias-dependent specific detectivity D*, as depicted in Figure 4d, achieves at room temperature. This performance not only surpasses commercial room-temperature thermal detectors (e. g., golay cell and pyroelectric sensors) by 2-3 orders of magnitude, but also exceeds the state-of-the-art $PtTe_2$-based detectors reported to date. A comprehensive comparison of $PtTe_2$ detectors employing different operational mechanisms is systematically summarized in Table 1, demonstrating 1-2 orders of magnitude enhancement in both responsivity and detectivity metrics compared to previously reported configurations.

3 Conclusions

Large-area high-quality $PtTe_2$ films were synthesized using a three-zone chemical vapor deposition (CVD) system, and THz detectors with varying channel lengths were fabricated through wet etching and standard photolithography processes. Characterization results demonstrate linear positive correlations between the device response and both bias voltage and incident power, alongside negative correlations between responsivity and channel length/operational frequency. These characteristics are attributed to the electromagnetic-induced potential well (EIW) mechanism. The EIW-based detectors exhibit a rapid response time of ~7.6 μs, enabling real-time THz imaging. Under limited bias conditions, the devices achieve optimal noise equivalent power (NEP) of 7.9×10^{-15} W/$Hz^{0.5}$ and specific detectivity (D*) of 9×10^{10} cm·$Hz^{0.5}$/W, representing the highest performance reported to date for $PtTe_2$-based detectors. The demonstrated scalability of large-area film synthesis provides a viable pathway for commercial applications of semimetal-based THz detectors.

表 1 与其他 $PtTe_2$ 探测器的性能比较

Table 1 Performance comparison with other $PtTe_2$ detectors

Mechanism	frequency	Responsivity	NEP	*D**	References
PTE	0.12–0.3 THz	~125 mA/W	60 pW/$Hz^{0.5}$	–	[28]
Photo galvanic effect & photon drag effect	0.1–1.5 THz	27.6 A/W	~5.8 pW/$Hz^{0.5}$	~ 5.3×10^9 cm·$Hz^{0.5}$/W	[29]
Free carrier absorption	0.02–0.3 THz	1.98 A/W	~47 pW/$Hz^{0.5}$	–	[30]
Asymmetrical coupling of the electrons with the THz	0.12 THz	3.8 A/W	–	–	[26]
EIW	0.02–0.173 THz	~10^3 A/W	7.9 fW/$Hz^{0.5}$	9×10^{10} cm·$Hz^{0.5}$/W	This Work

References

[1] Salén P, Basini M, Bonetti S, et al. Matter manipulation with extreme terahertz light: Progress in the enabling THz technology [J]. Physics Reports-Review Section of Physics Letters, 2019, 836: 1-74.

[2] Xu C, Ren Z, Wei J, et al. Reconfigurable terahertz metamaterials: From fundamental principles to advanced 6G applications [J]. iScience, 2022, 25(2): 103799.

[3] Zhong S C. Progress in terahertz nondestructive testing: A review [J]. Frontiers of Mechanical Engineering, 2019, 14(3): 273-81.

[4] Zaytsev K I, Dolganova I N, Chernomyrdin N V, et al. The progress and perspectives of terahertz technology for diagnosis of neoplasms: a review [J]. Journal of Optics, 2020, 22(1): 013001.

[5] Yan Z Y, Zhu L G, Meng K, et al. THz medical imaging: from in vitro to in vivo [J]. Trends in Biotechnology, 2022, 40(7): 816-30.

[6] Afsah-Hejri L, Hajeb P, Ara P, et al. A Comprehensive Review on Food Applications of Terahertz Spectroscopy and Imaging [J]. Comprehensive Reviews in Food Science and Food Safety, 2019, 18(5): 1563-621.

[7] Xue B A I, Zi-Yu Z, Lei-Jun X U, et al. High responsivity Terahertz detector linear array based on CMOS [J]. Journal of Infrared and Millimeter Waves, 2024, 43(1): 90-8.

[8] Ryou J, Kim Y-S, Kc S, et al. Monolayer MoS_2 Bandgap Modulation by Dielectric Environments and Tunable Bandgap Transistors [J]. Scientific Reports, 2016, 6(1): 29184.

[9] Deng B, Tran V, Xie Y, et al. Efficient electrical control of thin-film black phosphorus bandgap [J]. Nature Communications, 2017, 8(1): 14474.

[10] Banszerus L, Schmitz M, Engels S, et al. Ultrahigh-mobility graphene devices from chemical vapor deposition on reusable copper [J]. Science Advances, 1(6): e1500222.

[11] Shekhar C, Nayak A K, Sun Y, et al. Extremely large magnetoresistance and ultrahigh mobility in the topological Weyl semimetal candidate NbP [J]. Nature Physics, 2015, 11(8): 645-+.

[12] Yao C-Y, Zhang L-B, Wei Y-D, et al. Broadband terahertz detector based on topological insulator heterojunction [J]. Journal of Infrared and Millimeter Waves, 2023, 42(3): 362-8.

[13] Kurebayashi H, Garcia J H, Khan S, et al. Magnetism, symmetry and spin transport in van der Waals layered systems [J]. Nature Reviews Physics, 2022, 4(3): 150-66.

[14] Yan M, Huang H, Zhang K, et al. Lorentz-violating type-II Dirac fermions in transition metal dichalcogenide $PtTe_2$ [J]. Nature Communications, 2017, 8(1): 257.

[15] Chang J F, Ko T J, Je M, et al. Layer Orientation-Engineered Two-Dimensional Platinum Ditelluride for High-Performance Direct Alcohol Fuel Cells [J]. Acs Energy Letters, 2021, 6(10): 3481-7.

[16] Bae D, Park K, Kwon H, et al. Mitrofanovite, Layered Platinum Telluride, for Active Hydrogen Evolution [J]. Acs Applied Materials & Interfaces, 2021, 13(2): 2437-46.

[17] Wang M J, Ko T J, Shawkat M S, et al. Wafer-Scale Growth of 2D $PtTe_2$ with Layer Orientation Tunable High Electrical Conductivity and Superior Hydrophobicity [J]. Acs Applied Materials & Interfaces, 2020, 12(9): 10839-51.

[18] Ko T-J, Han S S, Okogbue E, et al. Wafer-scale 2D $PtTe_2$ layers-enabled Kirigami heaters with superior mechanical stretchability and electro-thermal responsiveness [J]. Applied Materials Today, 2020, 20: 100718.

[19] Kim S H, Kang M S, Choi J W, et al. Thickness-Dependent In-Plane Thermoelectric Properties of $PtTe_2$ with n-Type Conduction [J]. Journal of Physical Chemistry C, 2023, 127(3): 1673-9.

[20] Mc Manus J B, Horvath D V, Browne M P, et al. Low-temperature synthesis and electrocatalytic application of large-area $PtTe_2$ thin films [J]. Nanotechnology, 2020, 31(37): 375601.

[21] Kireev D, Okogbue E, Jayanth R T, et al. Multipurpose and Reusable Ultrathin Electronic Tattoos Based on $PtSe_2$ and $PtTe_2$ [J]. Acs Nano, 2021, 15(2): 2800-11.

[22] Okogbue E, Ko T J, Han S S, et al. Wafer-scale 2D $PtTe_2$ layers for high-efficiency mechanically flexible electro-thermal smart window applications [J]. Nanoscale, 2020, 12(19): 10647-55.

[23] Lin M-K, Villaos R A B, Hlevyack J A, et al. Dimensionality-Mediated Semimetal-Semiconductor Transition in Ultrathin $PtTe_2$ Films [J]. Physical Review Letters, 2020, 124(3): 036402.

[24] Xu H, Wei J, Zhou H, et al. High Spin Hall Conductivity in Large-Area Type-II Dirac Semimetal $PtTe_2$ [J]. Advanced Materials, 2020, 32(17): 2000513.

[25] Zeng L, Wu D, Jie J, et al. Van der Waals Epitaxial Growth of Mosaic-Like 2D Platinum Ditelluride Layers for Room-Temperature Mid-Infrared Photodetection up to 10.6 μm [J]. Advanced Materials, 2020, 32(52): 2004412.

[26] Xu H, Guo C, Zhang J, et al. $PtTe_2$-Based Type-II Dirac Semimetal and Its van der Waals Heterostructure for Sensitive Room Temperature Terahertz Photodetection [J]. Small, 2019, 15(52): 1903362.

[27] Yu W Z, Dong Z, Mu H R, et al. Wafer-Scale Synthesis of 2D Dirac Heterostructures for Self-Driven, Fast, Broadband Photodetectors [J]. Acs Nano, 2022, 16(8): 12922-9.

[28] Zhang K, Xing H, Wang L. $PtTe_2$-based terahertz photodetector integrated with an interdigital antenna [J]. Infrared Physics & Technology, 2022, 123: 104168.

[29] Jakhar A, Arya D S, Ghosh S, et al. Zero-Biased and Broadband (0.1 - 1.5 THz) Terahertz Detector Using Dirac Semimetal-Platinum Telluride ($PtTe_2$) [J]. IEEE Sensors Letters, 2022, 6(7): 1-4.

[30] Dong Z, Yu W, Zhang L, et al. Wafer-scale patterned growth of type-II Dirac semimetal platinum ditelluride for sensitive room-temperature terahertz photodetection [J]. InfoMat, 2023, 5(5): e12403.

[31] Zhang L, Guo C, Kuo C-N, et al. Terahertz Photodetection with Type-II Dirac Fermions in Transition-Metal Ditellurides and Their Heterostructures [J]. physica status solidi (RRL) - Rapid Research Letters, 2021, 15(8): 2100212.

[32] Suo P, Yan S N, Pu R H, et al. Ultrafast photocarrier and coherent phonon dynamics in type-II Dirac semimetal $PtTe_2$ thin films probed by optical spectroscopy [J]. Photonics Research, 2022, 10(3): 653-61.

[33] XU Xin-Yue, ZHANG Xiao-Dong, WU Jing, et al. High responsivity Bi_2Te_3-based room temperature terahertz detector based on metal-semiconductor-metal (MSM) structure [J]. Journal of Infrared and Millimeter Waves, 2019, 38(4): 459-63.
(徐新月, 张晓东, 吴敬, 等. 基于金属-半导体-金属结构的Bi_2Te_3室温高响应率太赫兹探测器 [J]. 红外与毫米波学报), 2019, 38(4): 459-63.

[34] Huang Z M, Zhou W, Tong J C, et al. Extreme Sensitivity of Room-Temperature Photoelectric Effect for Terahertz Detection [J]. Advanced Materials, 2016, 28(1): 112-+.

[35] Huang Z M, Tong J C, Huang J G, et al. Room-Temperature Photoconductivity Far Below the Semiconductor Bandgap [J]. Advanced Materials, 2014, 26(38): 6594-8.